Supplementary Information (SI) for Energy & Environmental Science.

Supporting Information

Ultra−Uniform Interfacial Matrix via High−Temperature Thermal Shock for Long−Cycle Stability Cathodes of Sodium-ion Batteries

Zekun Li, [a] Pengfei Huang, [a, c] Jinfeng Zhang, [a] Zhaoxin Guo, [a] Zhedong Liu, [a] Li Chen, [a] Jingchao Zhang, [a] Jiawei Luo, [a] Xiansen Tao, [e] Zhikai Miao, [a] Haoran Jiang, [a] Chunying Wang, [a] Xinran Ye, [a] Xiaona Wu, [b] Wei-Di Liu, [d] Rui Liu, [b] Yanan Chen, [a,*] Wenbin Hu, [a,*]

[a] School of Materials Science and Engineering, Tianjin University, Tianjin, 300072 China.

[b] School of Materials Science and Engineering, Shandong University of Science and Technology, Qingdao 266590, China.

[c] Key Laboratory of Coal Processing and Efficient Utilization of Ministry of Education, China University of Mining and Technology, Xuzhou 221116, Jiangsu, China.

[d] School of Chemistry and Physics (Faculty of science), ARC Research Hub in Zero−emission Power Generation for Carbon Neutrality, and Centre for Materials Science, Queensland University of Technology, Brisbane, QLD 4000.

[e] School of Chemistry, Chemical Engineering and Materials, Jining University, Qufu 273155, China.

Experimental section

Preparation of materials: To produce spherical $NaNi_{1/3}Fe_{1/3}Mn_{1/3}(OH)_2$ precursors, a calculated combination of nickel sulfate hexahydrate ($NiSO_4·6H_2O$), iron sulfate heptahydrate ($FeSO_4·7H_2O$), and manganese sulfate monohydrate ($MnSO_4·H_2O$) was dissolved in water, resulting in a transition metal solution with a 2 mol L^{-1} concentration. A separate 10 mol L^{-1} NaOH and 1.5 mol L^{-1} NH_4OH solution was prepared to regulate the pH and serve as a chelating agent. The transition metal sulfate solution was continuously introduced into a 10−liter continuously stirred tank reactor (CSTR) with a stirring speed of 600 rpm under a nitrogen atmosphere, maintaining a reaction temperature of 50°C and automatically controlling the pH between 10.8 and 11.0. As the sulfate solution was consumed, $Ni_{1/3}Fe_{1/3}Mn_{1/3}(OH)_2$ precursors were formed. These hydroxide precursors were filtered, washed, and dried in air for 48 hours. The dried precursors were then mixed with Na_2CO_3 powder in a stoichiometric ratio with a 5 mol %excess of sodium and immediately stored in an argon−filled glove box for further processing. The $NaNi_{1/3}Fe_{1/3}Mn_{1/3}(OH)_2$ precursors, sifted through a 400−mesh sieve, were combined with Na_2CO_3 that had also been sifted through a 400−mesh sieve. The mixture was placed in a sealed container and agitated using a planetary shaker for a duration of 10 minutes. Subsequently, this mixture was combined with ethanol in a beaker and stirred continuously until the ethanol evaporated. The resulting substance was dried to form a powder. This powder underwent calcination at 835°C for 15 hours with a heating rate of 5 °C min^{-1} in a tube furnace under an oxygen atmosphere, culminating in the formation of the final material, $NaNi_{1/3}Fe_{1/3}Mn_{1/3}O_2$, referred to as Tu−333. For comparison, the mixtures were uniformly spread on nickel foil with dimensions of 2 cm by 5 cm. The mixtures coated on the nickel foil were calcined at 835 °C for 60 seconds in a high−temperature synthesis (HTS) setup under an oxygen environment, with the HTS equipment provided by Shenzhen Zhongkejingyan. This procedure was reiterated to produce the positive electrode material labeled HT−333. In a similar manner, $Ni_{1/3}Fe_{1/3}Mn_{1/3}(OH)_2$ precursors were combined with stoichiometric amounts of Na_2CO_3, $Ca(OH)_2$, and $NH_4H_2PO_4$, followed by stirring in anhydrous ethanol for 60 minutes. Subsequently, the mixture was dried at 90 °C. The resultant powder was then calcined using both a tube furnace and HTS approaches, resulting in products denoted as Tu−NCP@333 and HT−NCP@333 , respectively.

Material characterization: The elemental compositions of these specimens were determined using inductively coupled plasma atomic emission spectroscopy (ICP−AES, Shimadzu, ICPS−8100). XRD measurements were carried out utilizing the Smartlab 9kW with Cu Kα radiation ($\lambda = 1.5406$ Å). The operating voltage and current were set to 40 kV and 15 mA, respectively. Sample morphology was analyzed using a thermal field SEM (JEOL, model JSM–7800F) and a TEM (JJEM−F200). T The "AtomSegNet" software offers a sophisticated tool for high-resolution image processing and accurate localization of atomic columns. This technology utilizes a deep learning-assisted algorithm designed for atomic-scale phase segmentation, crucial for distinguishing between O3 and rock salt phase structures. Elemental chemical state analysis was conducted using XPS spectra from Shimadzu/Krayos AXIS Ultra DLD. FTIR spectra were recorded with an IR spectrometer (Thermo Fisher iS10) at ambient temperature. Ex−situ X−ray absorption spectroscopy (XAS) spectra at the Fe and Ni K−edge were collected at Beamline 11B of the Shanghai Synchrotron Radiation Facility (SSRF). The extended X−ray absorption fine structure (EXAFS) region was k^3 weighted and Fourier transformed within the k range of 2.5−10.0 Å^{-1}.

Electrochemical measurement: All electrochemical tests are based on three times measurements. Coin cells (CR2032) were assembled in argon−filled glove box. Cathode films were produced by combining 80 wt% of the active material, 10 wt% carbon nanotubes, and 10 wt% polytetrafluoroethylene within a glovebox environment. These mixtures were subsequently rolled to create self−supporting films, with the active material having a loading mass of 8–10 mg cm^{-2}. Na metal and glass fiber were used as anodes and separators, respectively. Pouch cells were assembled. Anodes are made from a slurry of HC material, Super P, and sodium alginate binder (90:5:5) in water. Cathodes were made by mixing 90 wt.% active material, 5 wt.% carbon black, and 5 wt.% PVDF in NMP solution. These slurries were double−sided coated onto 12 μm Al foils to achieve a mass loading of 10^{-12} mg/cm^2. The samples were cut to dimensions of 6.98×9 cm^2 and 6.68×8.7 cm^2, respectively, resulting in an N/P capacity ratio of 1.1. The electrolyte consisted of 1.0 M NaPF$_6$ in a mixture of ethylene carbonate and diethyl carbonate (EC: DEC) in a 1:1 ratio. A Celgard 3501 separator and aluminum plastic film for packaging were employed. The lithium−ion storage performance and Galvanostatic Intermittent Titration Technique (GITT) assessments were executed using a Neware battery testing device, with the voltage range set between 0.01 and 3.00 V versus Li$^+$/Li. Calculation of Na$^+$ diffusion coefficients through GITT results: As the Na$^+$ transportation in the electrode materials follows Fick's second law, the apparent Na$^+$ chemical diffusion coefficients (D$_{Na+}$) in the single−phase regions can be calculated by:

$$D = \frac{4}{\pi\tau}\left(\frac{n_{m}V_{m}}{M_{B}S}\right)^2\left(\frac{\Delta E_{S}}{\Delta E_{\tau}}\right)^2 \qquad (1)$$

where M$_B$ represents the mass of the cathode material in the electrode, V$_M$ represents the molar volume of material, M_B represents the molecular weight of material, S is the active surface area between electrolyte and electrode, ΔE_S is the difference of the steady−state voltage of cell for the rest, and $\Delta E\tau$ is the total transient voltage difference of the cell for applied current for time τ. τ is the time duration in which the current is applied, and L is the diffusion distance of Na^+ from lattice to liquid electrolyte. Cyclic voltammetry (CV) profiles and impedance spectroscopy data were acquired at various scan rates through a CHI electrochemical workstation.

DFT Computational: Computations were executed utilizing the Vienna Ab initio Simulation Package (VASP) and the generalized gradient approximation (GGA) method supplemented by the Perdew−Burke−Ernzerhof (PBE) exchange−correlation functional. Partial occupation scenarios for Ni, Mn, and Fe were simulated employing the enumlib package to create disorder configurations. The interaction between nuclei and extranuclear electrons was modeled through the projector augmented wave (PAW) method. Spin polarizations were incorporated consistently across all computational analyses. The cut−off energies were stipulated as 520 eV for the wave function and 780 eV for the density. The Hubbard U parameters were assigned as follows: 3.9 eV for Ni, 5.3 eV for Mn, and 7.0 eV for Fe, respectively. A k−mesh density of one point per 0.02 Å was employed. Convergence criteria for energy and forces were defined at 1×10^{-6} eV and 0.01 eV/Å, respectively. For geometric optimization, a 2 × 2 × 2 Monkhorst−Pack mesh with appropriate K−point sampling of Brillouin−zone integrals was utilized, whereas a 4 × 4 × 5 mesh was engaged to determine electronic properties. The computations adopted the DFT+U methodology with U set at 4 eV.

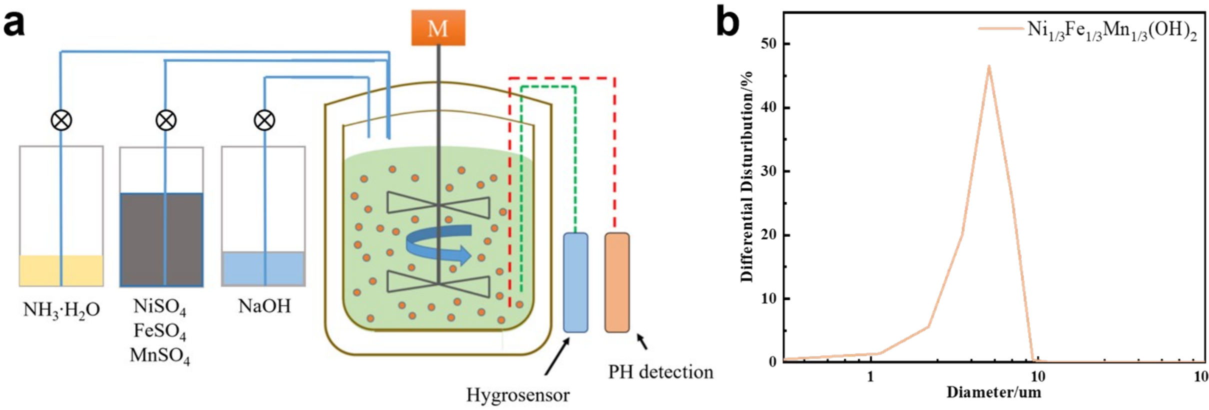

Fig. S1. a). Schematic diagram of the co-precipitation reaction process. b). Particle size distribution of the $Ni_{1/3}Fe_{1/3}Mn_{1/3}(OH)_2$ precursors.

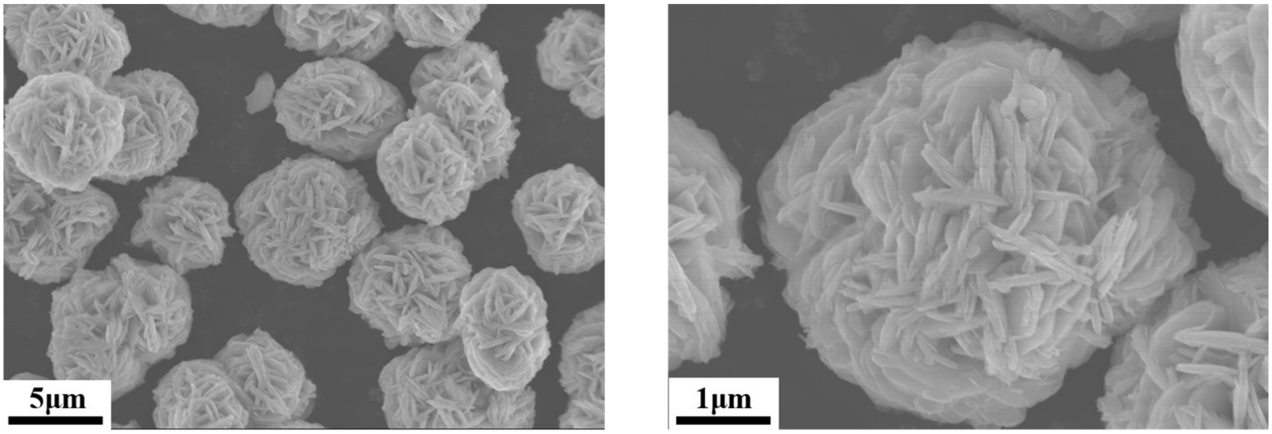

Fig. S2. SEM image for $Ni_{1/3}Fe_{1/3}Mn_{1/3}(OH)_2$ precursors.

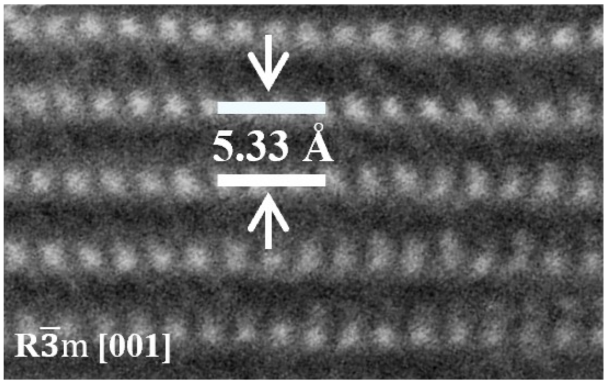

Fig. S3. STEM-HAADF image of HTS-NCP@333.

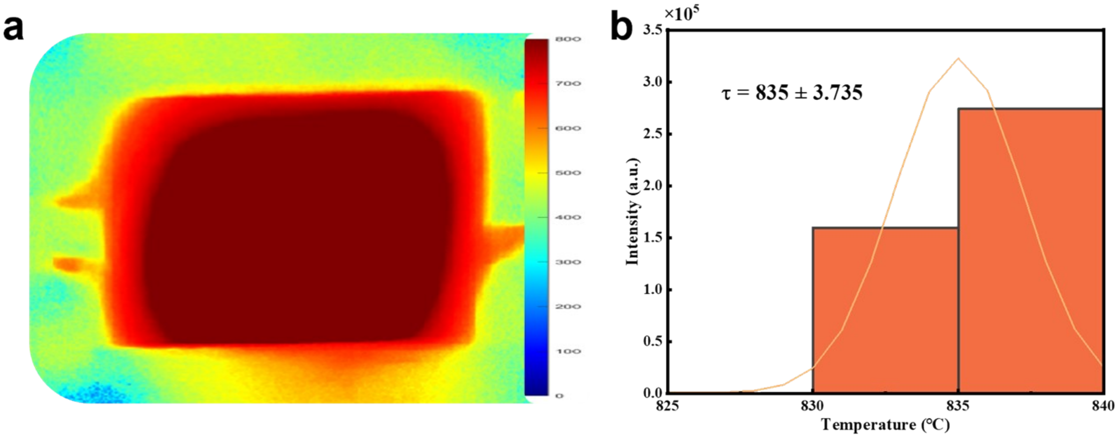

Fig. S4. a) Thermal radiation diagram of HT-NCP@333 during the synthesis process and b) Temperature test distribution (bars) and trend curve (orange line).

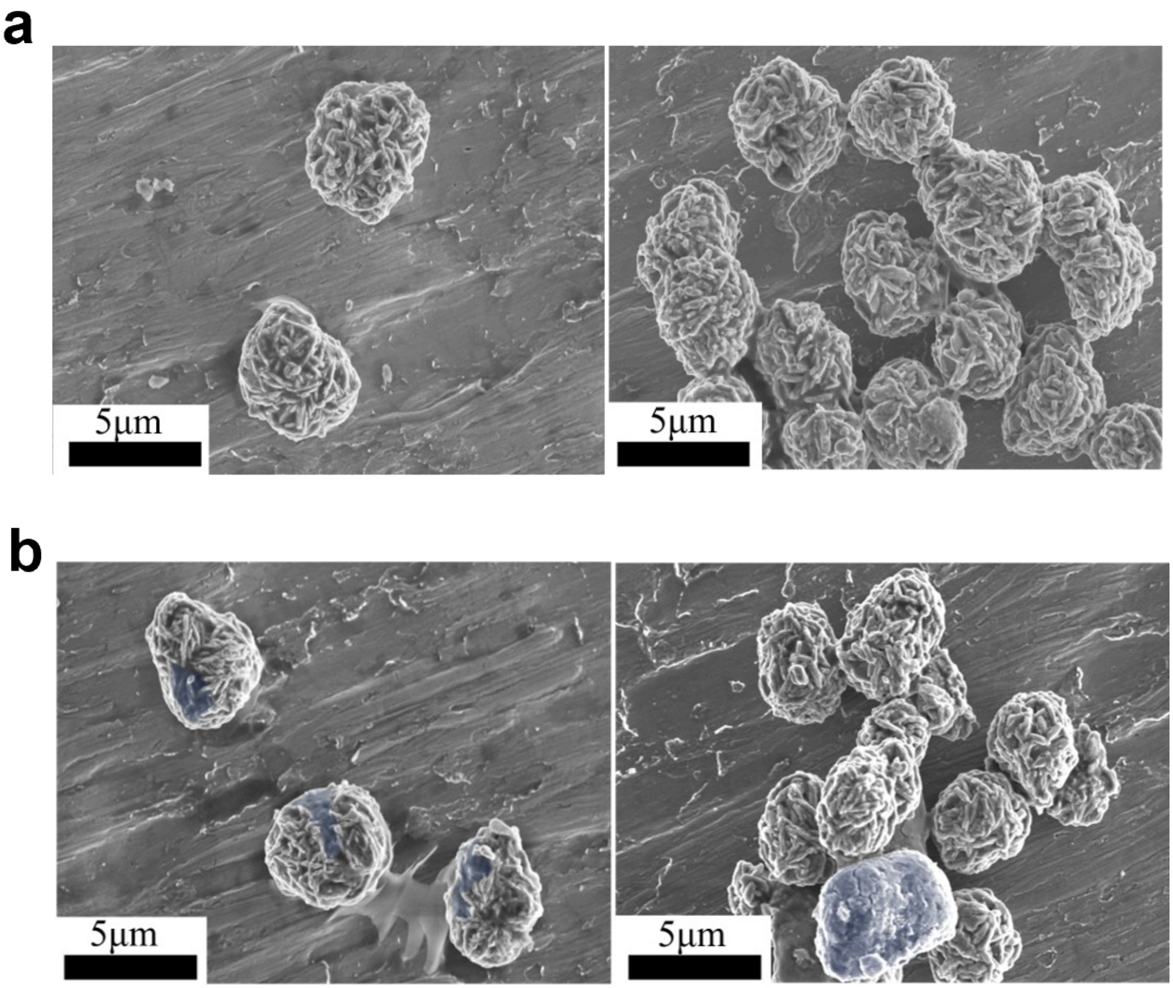

Fig. S5. SEM images with corresponding magnification for a) HT-NCP@333 and b) Tu-NCP@333 (light blue area represents surface defects).

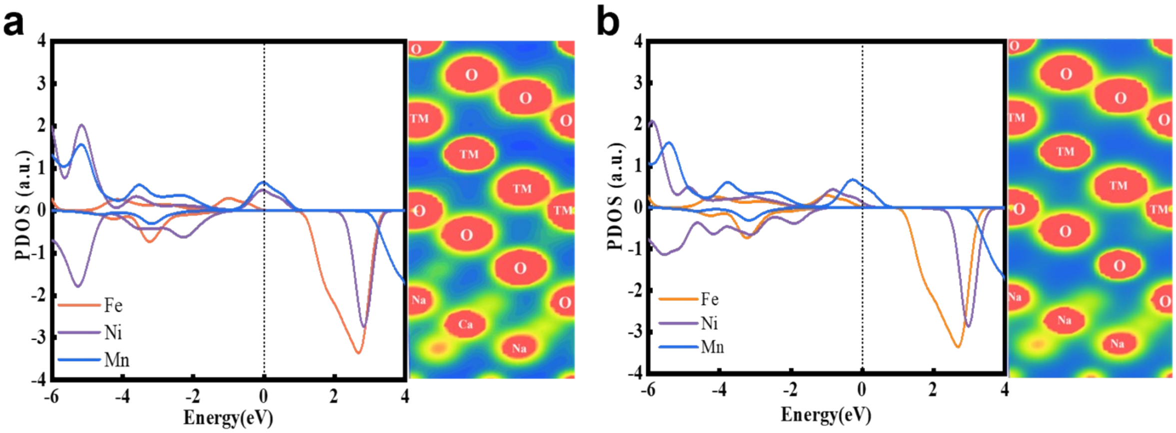

Fig. S6. Calculated projected density of states of TMs and sliced isosurface of a) Ca-NFM333 and b) NFM333.

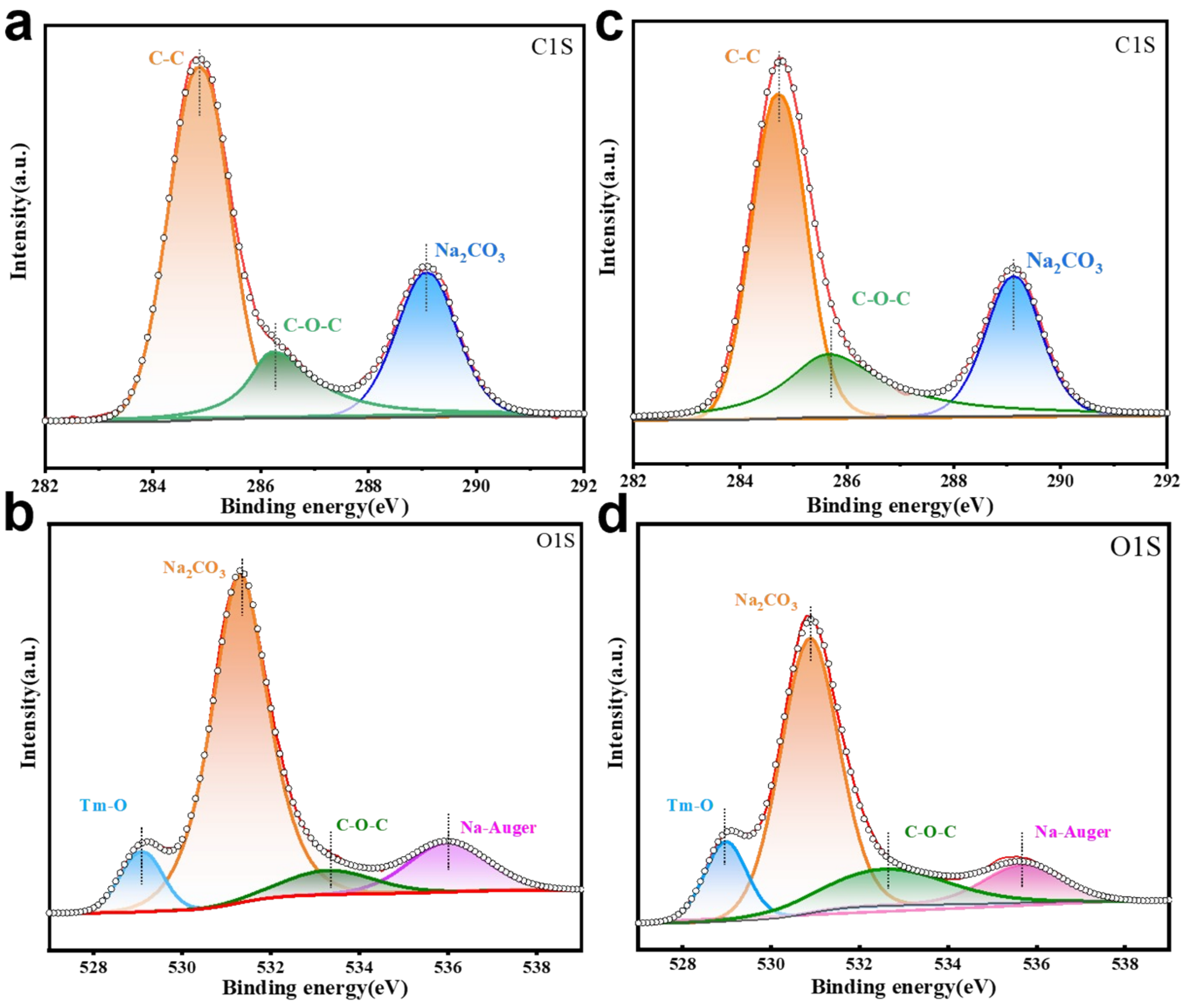

Fig. S7. (a, b) XPS spectra of C 1s and O 1s of HT-NCP@333, and (c, d) C 1s and O 1s of Tu-NCP@333.

Fig. S8. Image of the alumina crucible surface post- calcination materials in a tube furnace: Tu-333 (Right) and Tu-NCP@333 (Left).

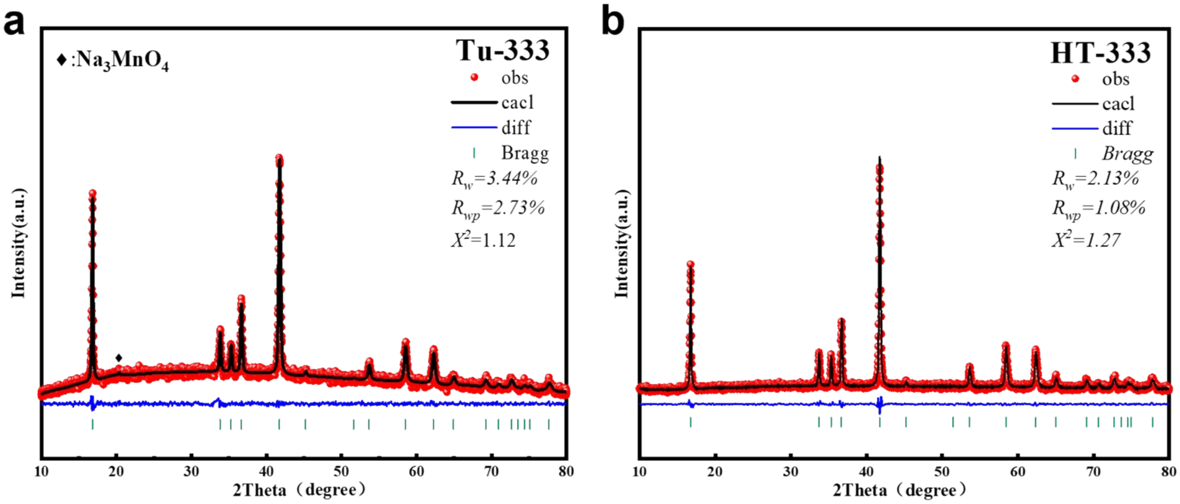

Fig. S9. XRD Rietveld refinement pattern of a) Tu-333 and b) HT-333.

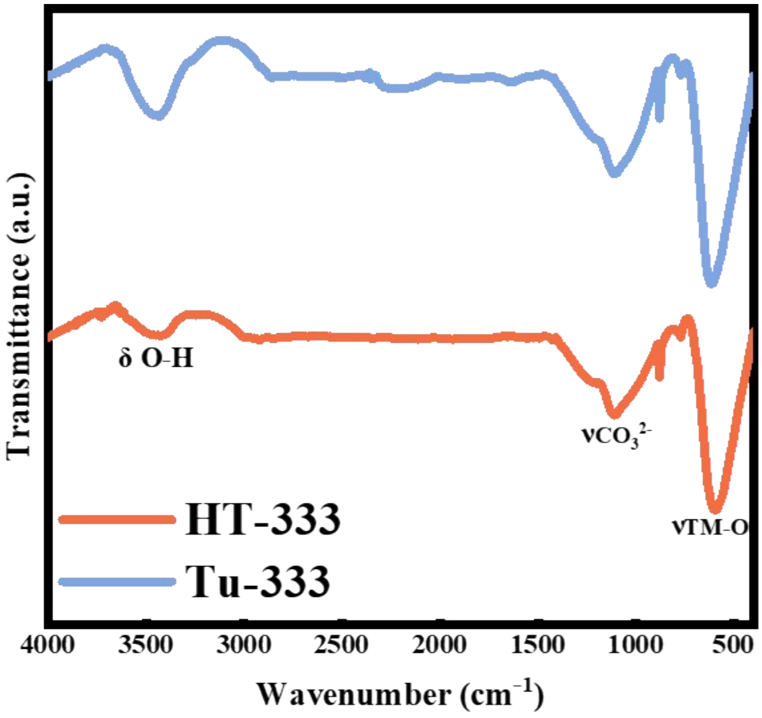

Fig. S10. The IR spec trum features bending and stretching vibrations of OH and $CO3^{2-}$, as well as the TM-O bands in HT-333 and Tu-333.

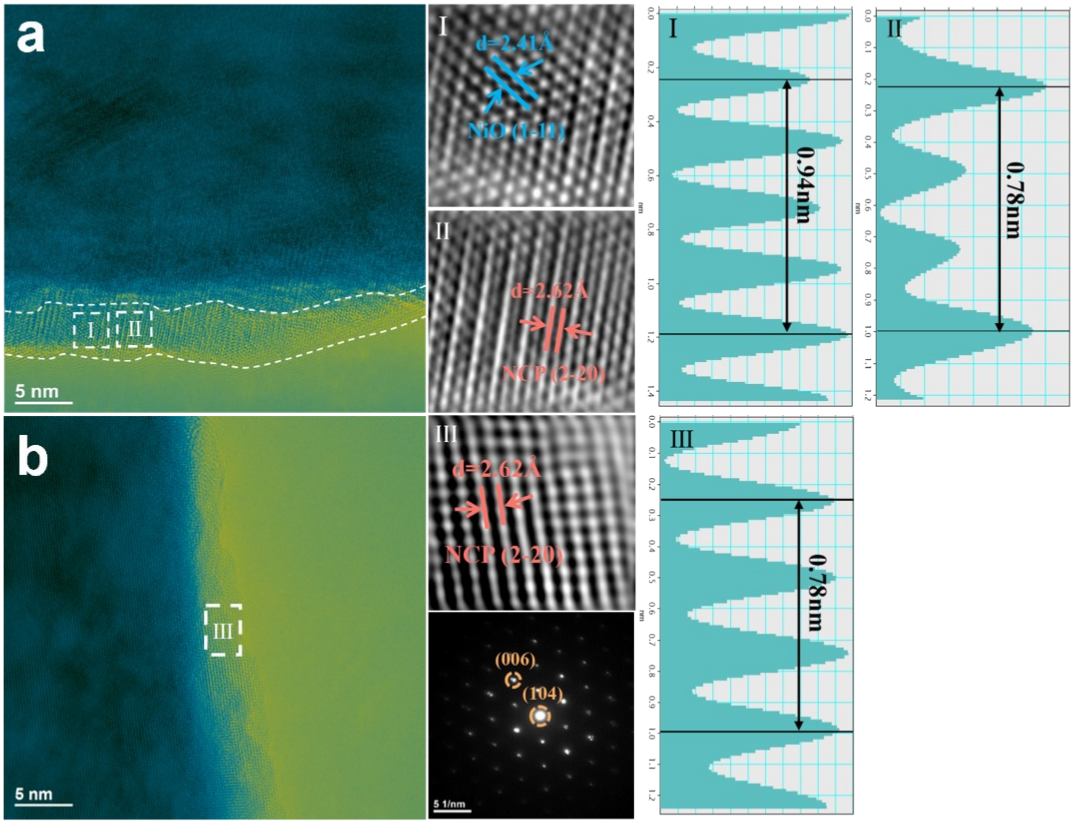

Fig. S11. High-resolution TEM images exhibit the distinct interfaces, with corresponding reduced fast Fourier transform (FFT) images and intensity line profiles for selected areas: a) HT-NCP@333 and b) Tu-NCP@333.

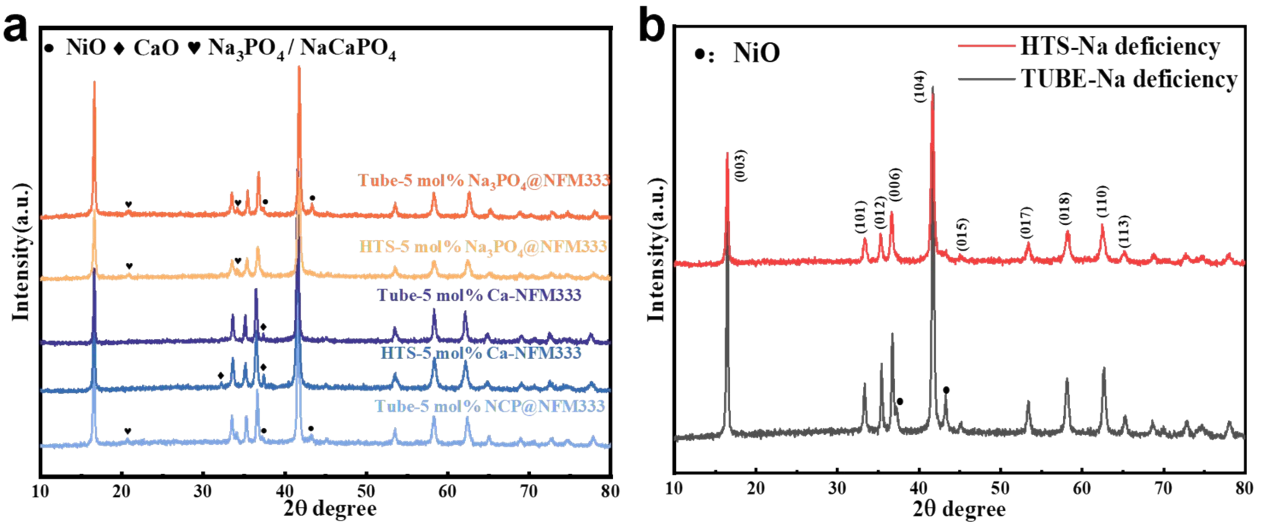

Fig. S12. a) XRD patterns of 5 mol % Na_3PO_4@NFM333, 5 mol % Ca dopped NFM333 and 5 mol % NCP@NFM333 synthesized by HTS and Tube. b) XRD patterns of $Na_{0.95}Ni_{1/3}Fe_{1/3}Mn_{1/3}O_2$ synthesized by HTS and Tube.

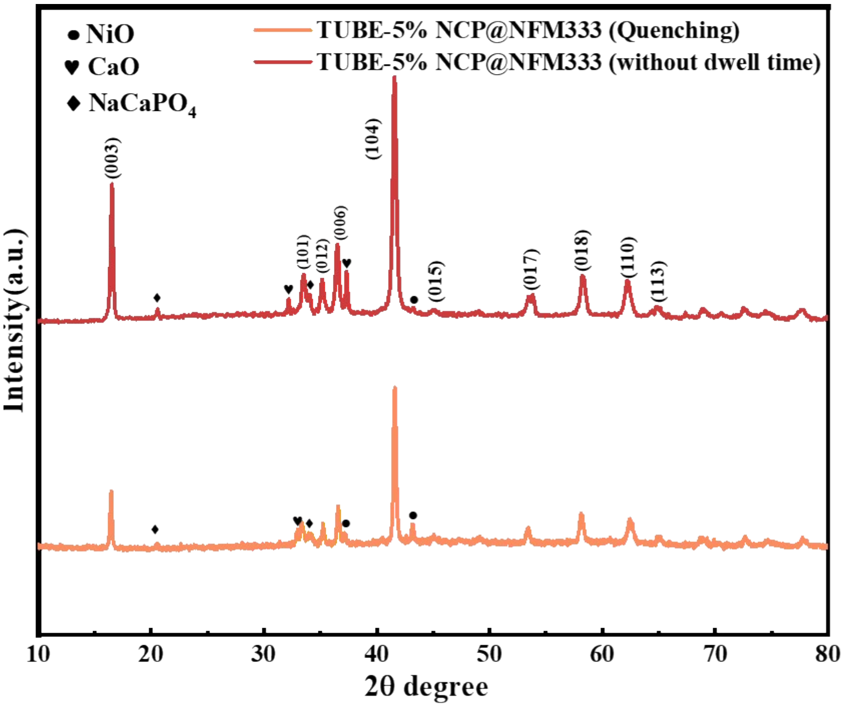

Fig. S13. Ex situ XRD patterns of 5 mol % NCP@NFM333 under rapid quenching and without dwell time conditions during the Tube process.

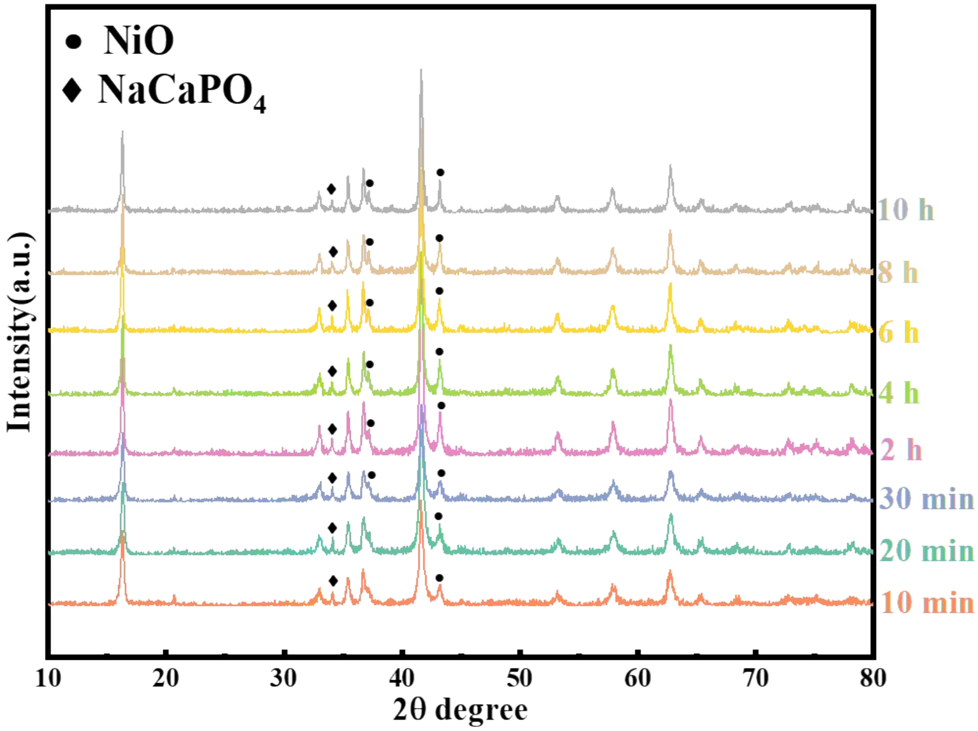

Fig. S14. XRD patterns evolution of 5mol% NCP@NFM333 in the Tube process over different insulation times.

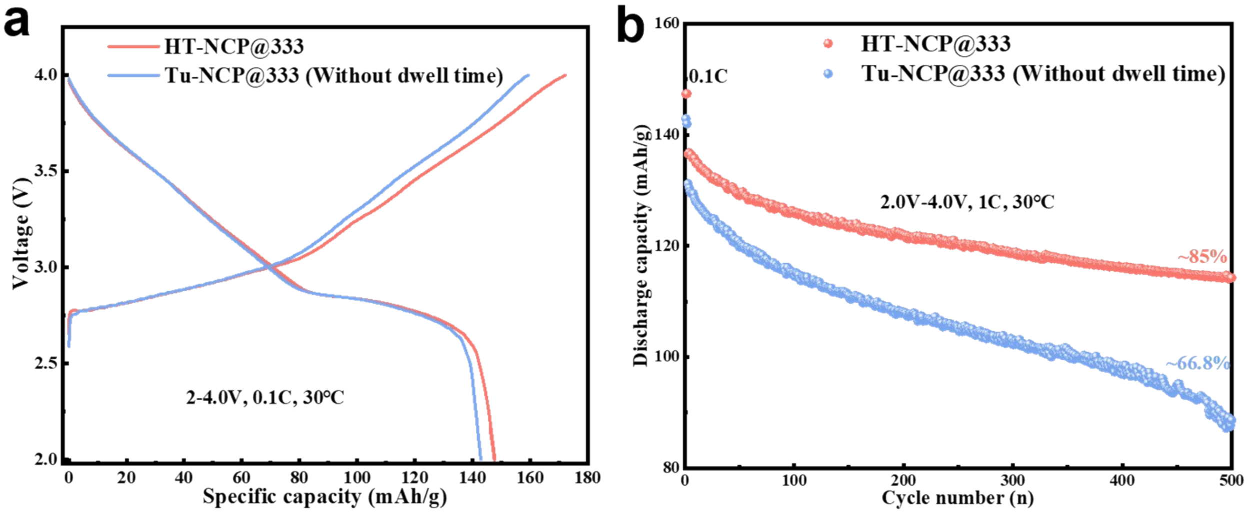

Fig. S15. a) Initial charge and discharge voltage profiles of HT-NCP@333 and Tu-NCP@333 without dwell time. b) Cycling performance for the two materials during 500 cycles at 1C in the voltage range of 2.0-4.0 V.

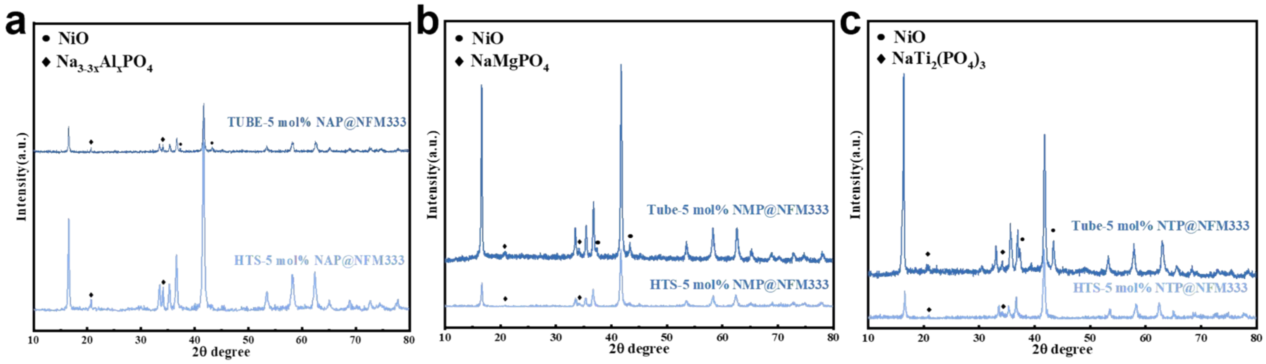

Fig. S16. XRD patterns of a) 5mol% NAP@NFM333. b) 5mol%NMP@NFM333. c) 5mol%NTP@NFM333 synthesized by HTS and Tube process.

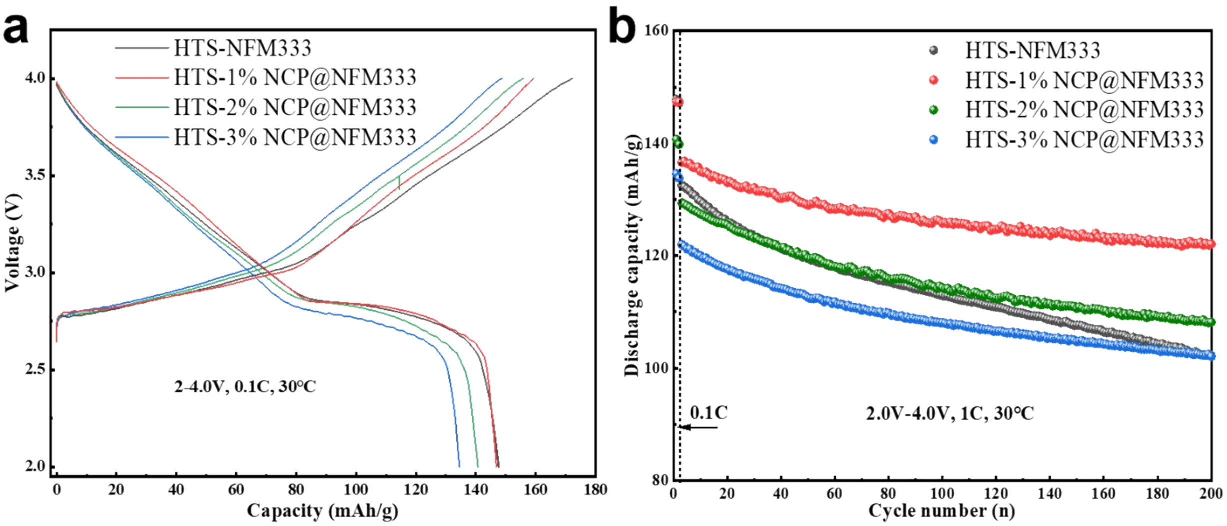

Fig. S17. a) The galvanostatic charge–discharge curves of HTS-NFM333 and 1mol%, 2mol% and 3mol% HTS-NCP@NFM333. b) Cycling performance during 200 cycles at 1C after the initial two cycles of activation at 0.1C in the voltage range of 2.0−4.0 V.

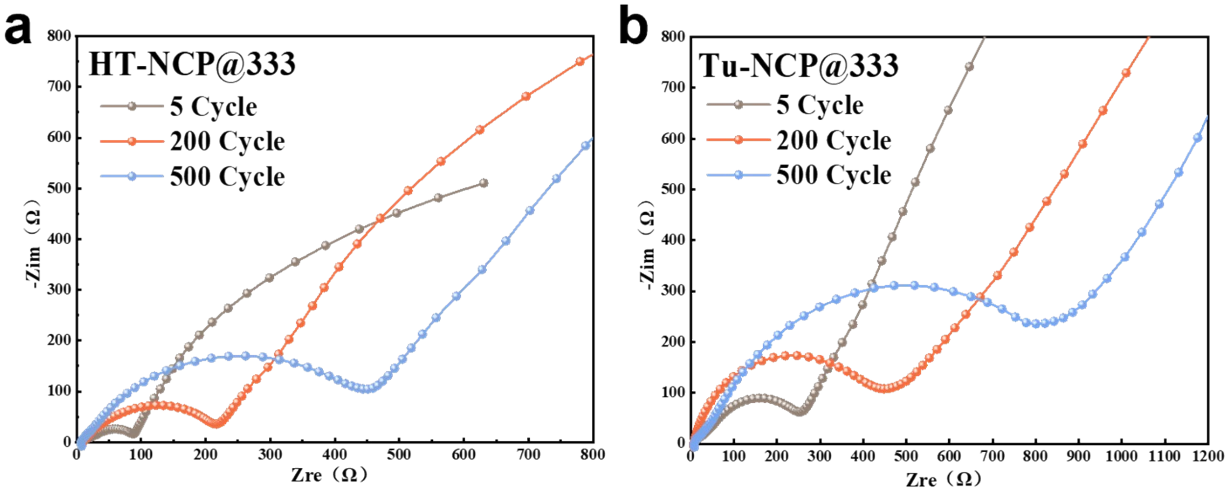

Fig. S18. Electrochemical impedance spectroscopy of the a) HT-NCP@333 and b) Tu-NCP@333 after 5, 200, and 500 cycles.

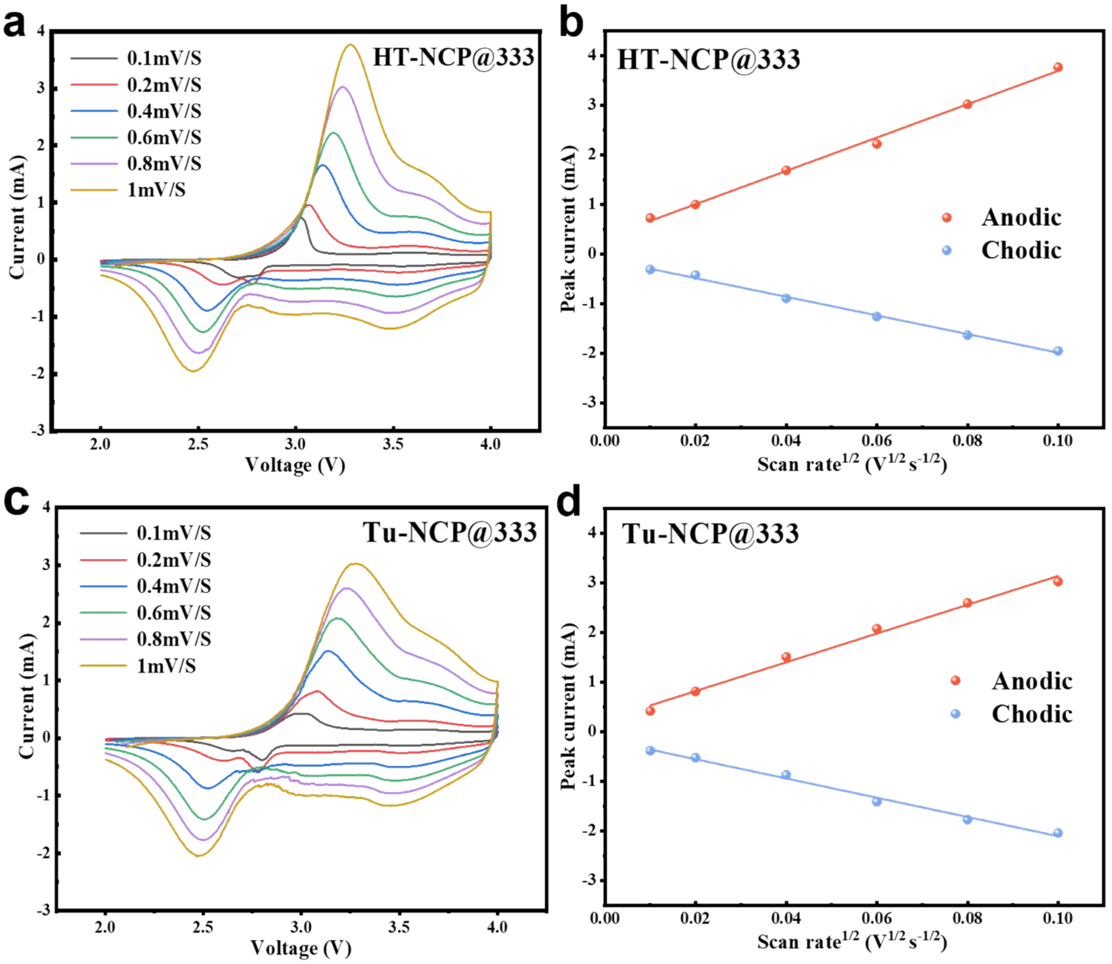

Fig. S19. a, c) CV curves of the HT-NCP@333 and Tu-NCP@333 electrodes under various sweep rates from 0.1 to 1.0 mV/s. b, d) Linear relationship of peak currents with the square root of scan rate $v^{1/2}$ of the HT-NCP@333 and Tu-NCP@333 obtained from the CV measurements.

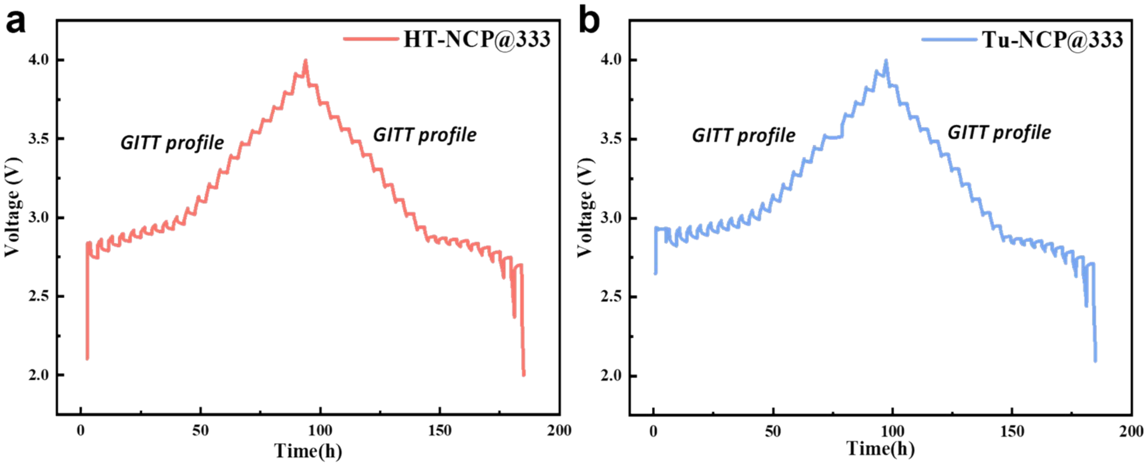

Fig. S20. a, b) GITT curves of the HT-NCP@333 and Tu-NCP@333 cathode materials in the first cycle.

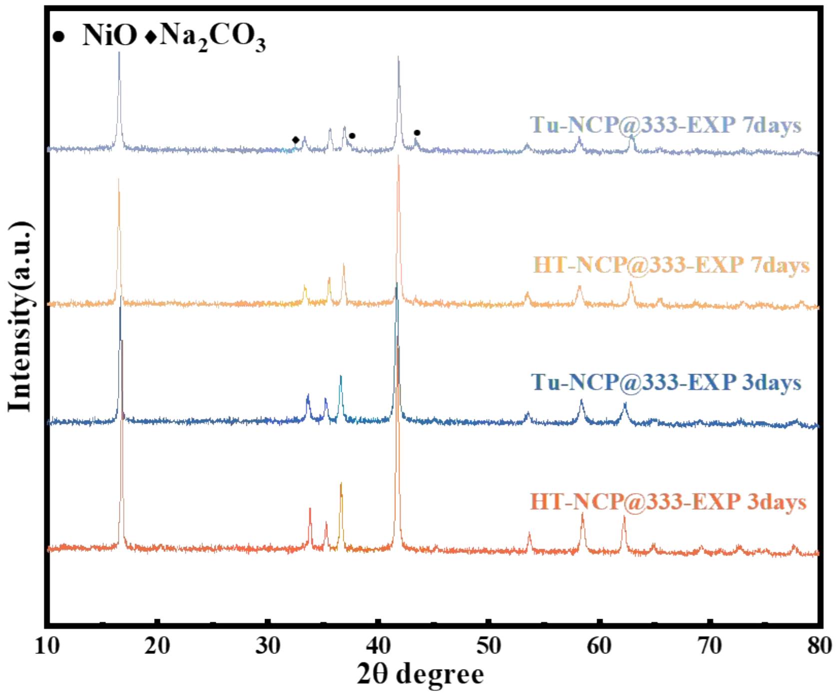

Fig. S21. XRD patterns of the HT-NCP@333 and Tu-NCP@333 powders after 3 days and 7 days exposure in RH~30% humidity environment.

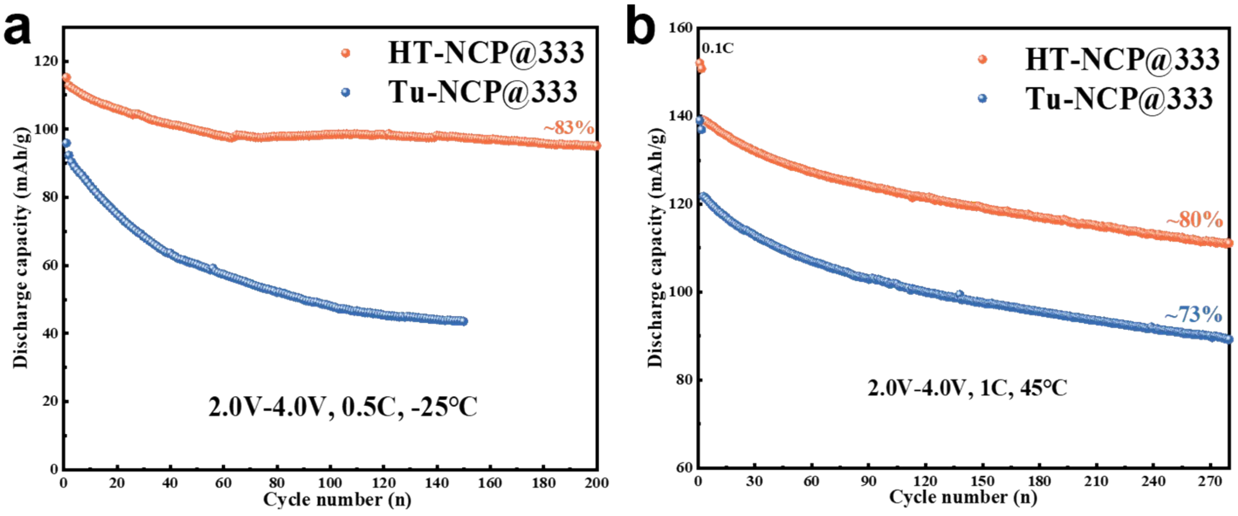

Fig. S22. a) Low-temperature cycling performance at -25 °C for HT-NCP@333 and Tu-NCP@333 in the voltage range of 2.0-4.0V. b) High-temperature cycling performance at 45 °C for HT-NCP@333 and Tu-NCP@333 in the voltage range of 2.0-4.0V.

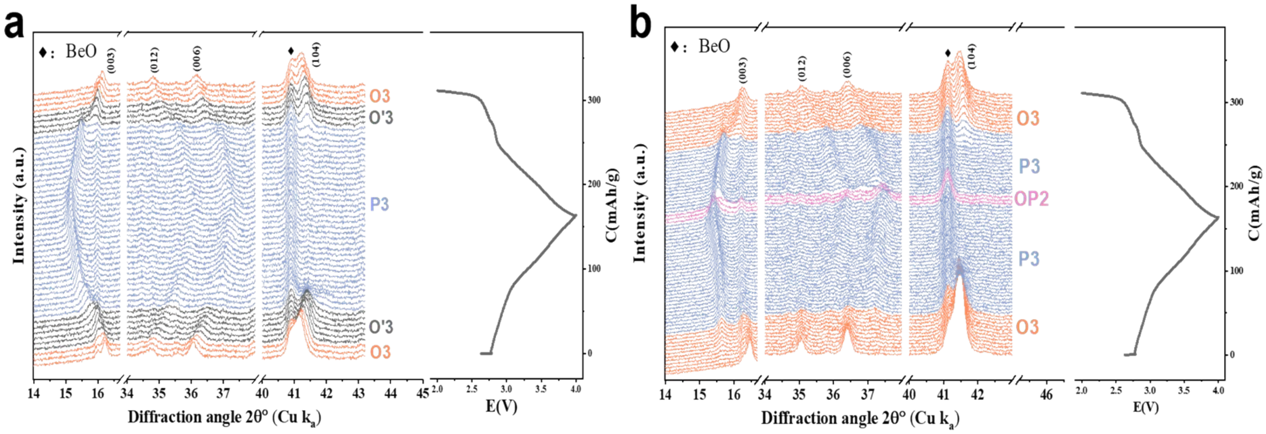

Fig. S23. Initial charge curves, in situ XRD patterns collected during the first cycle at 0.1 C within the voltage range of 2.0-4.0 V for a) Tu-NCP@333 and b) HT-NCP@333.

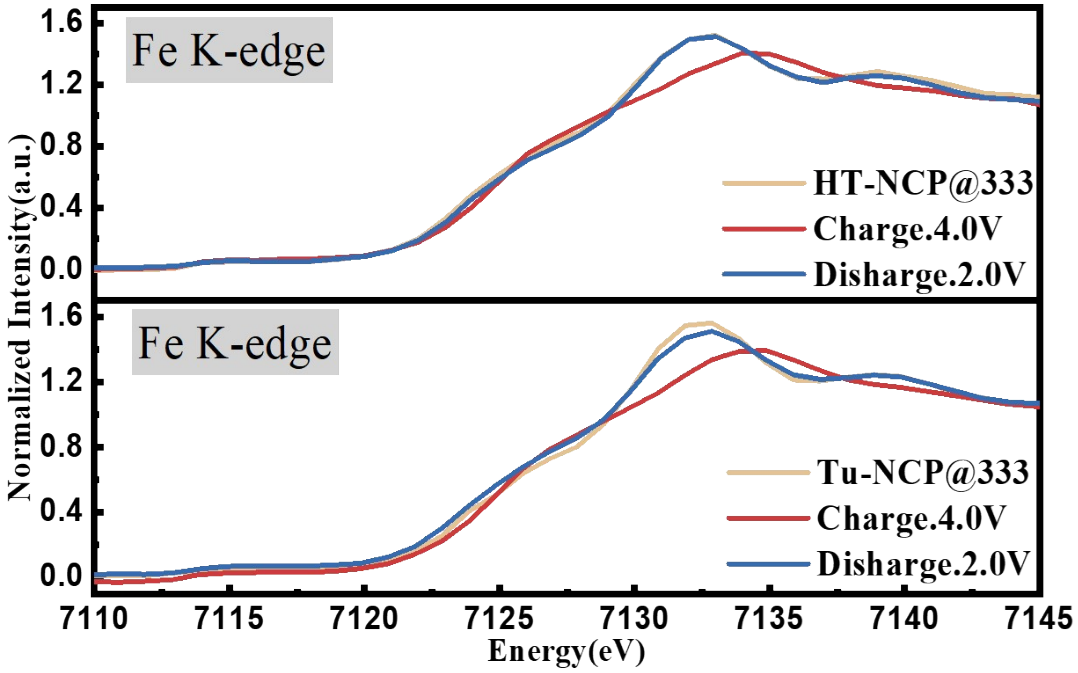

Fig. S24. X-ray absorption near-edge structure of Fe K edge of Tu-NCP@333 and HT-NCP@333 during first charge and discharge.

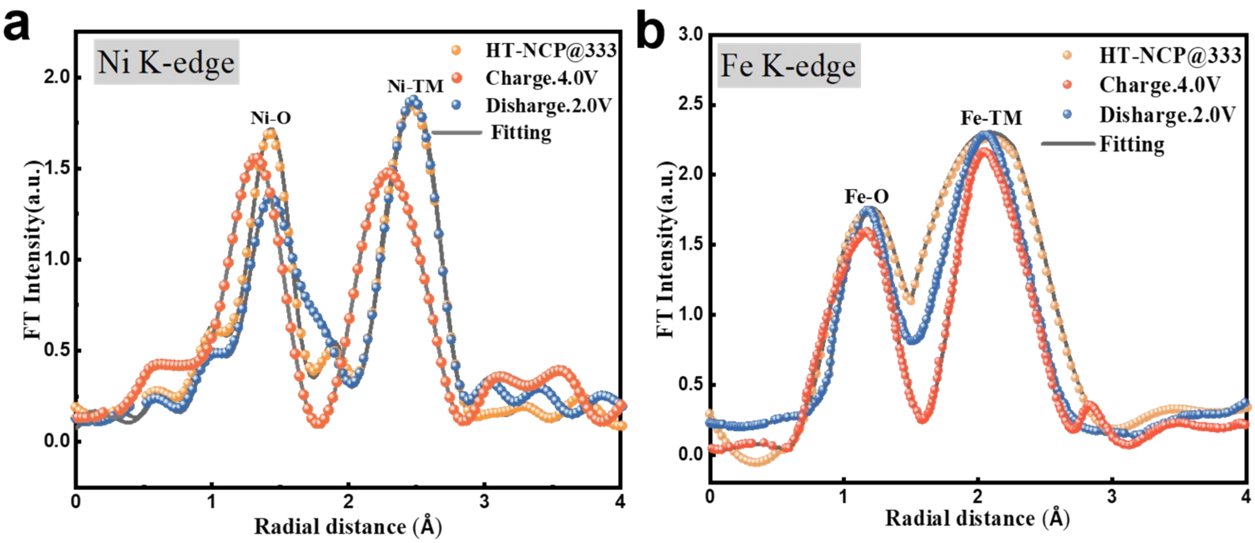

Fig. S25. a) Ni K-edge and b) Fe K-edge ex situ EXAFS spectra and fitting for HT-NCP@333 at different charge/discharge states.

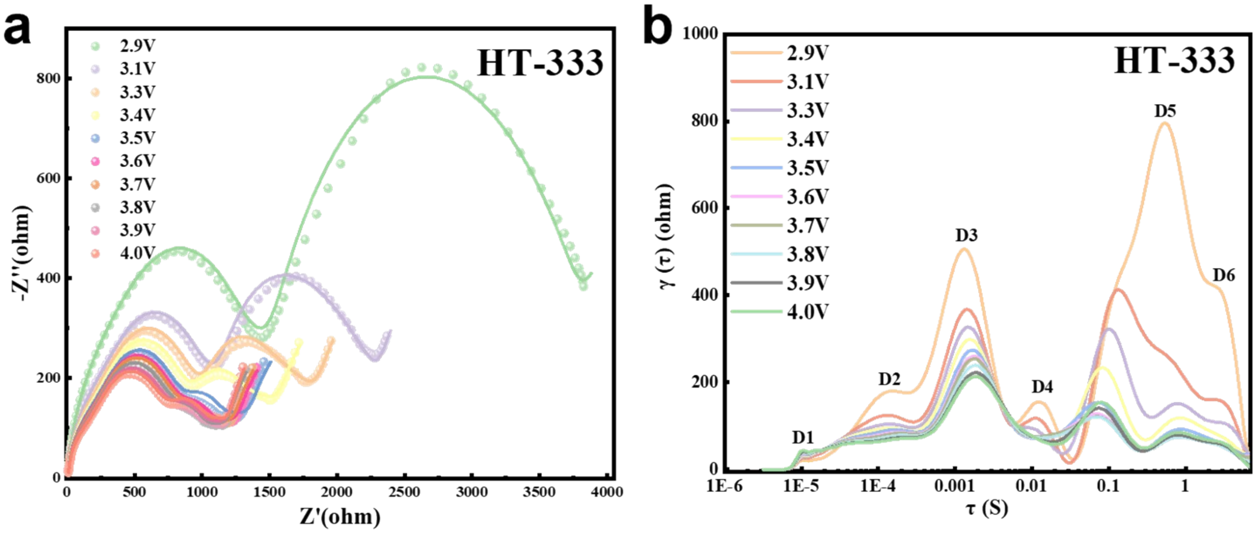

Fig. S26. a) The in situ EIS and fitting analysis of HT− 333. b) Corresponding in situ DRT analysis of HT− 333 during charge and discharge processes.

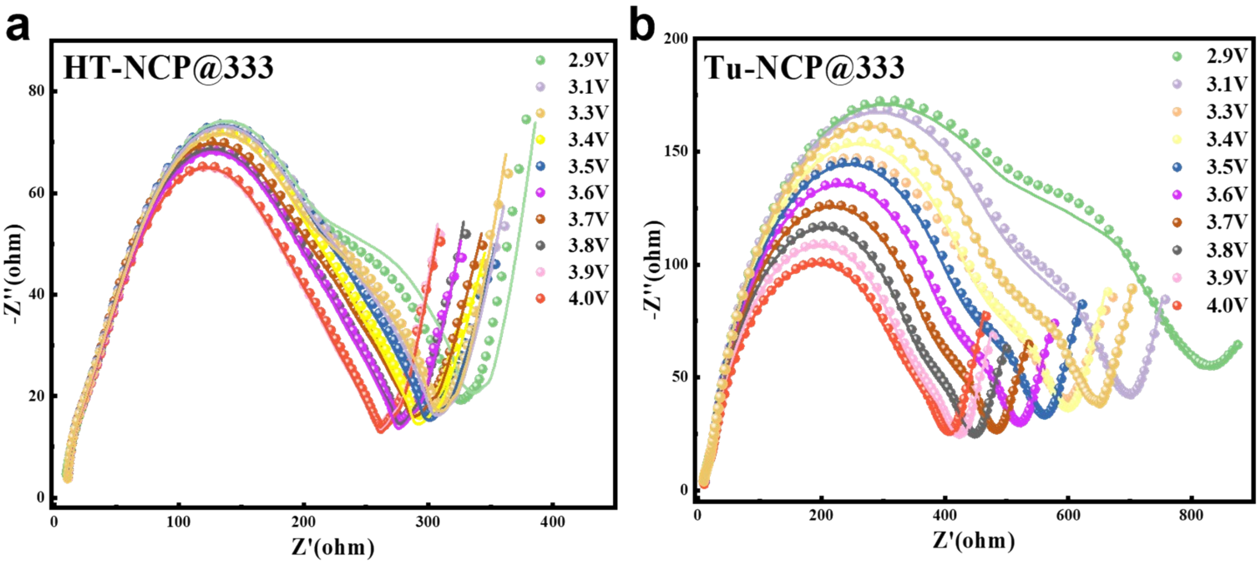

Fig. S27. The in situ EIS and fitting analysis of a) HT-NCP@333 and b) Tu-NCP@333 during charge and discharge processes.

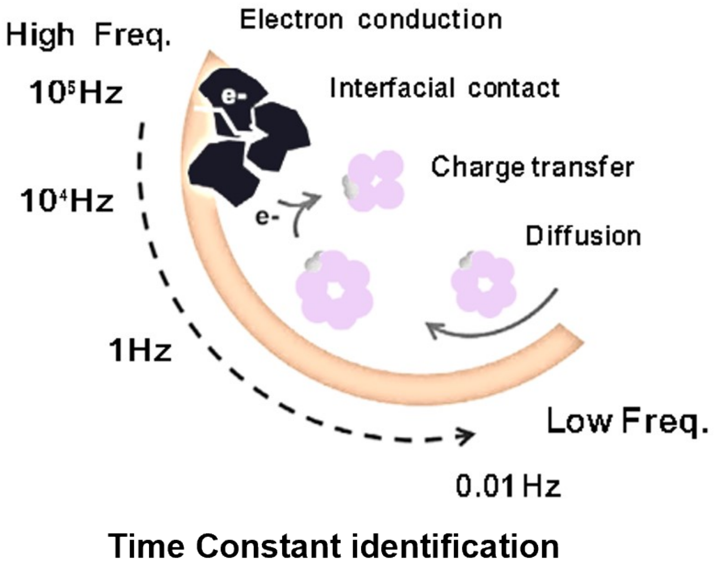

Fig. S28. Schematic of frequency range analysis and time constant identification in EIS.

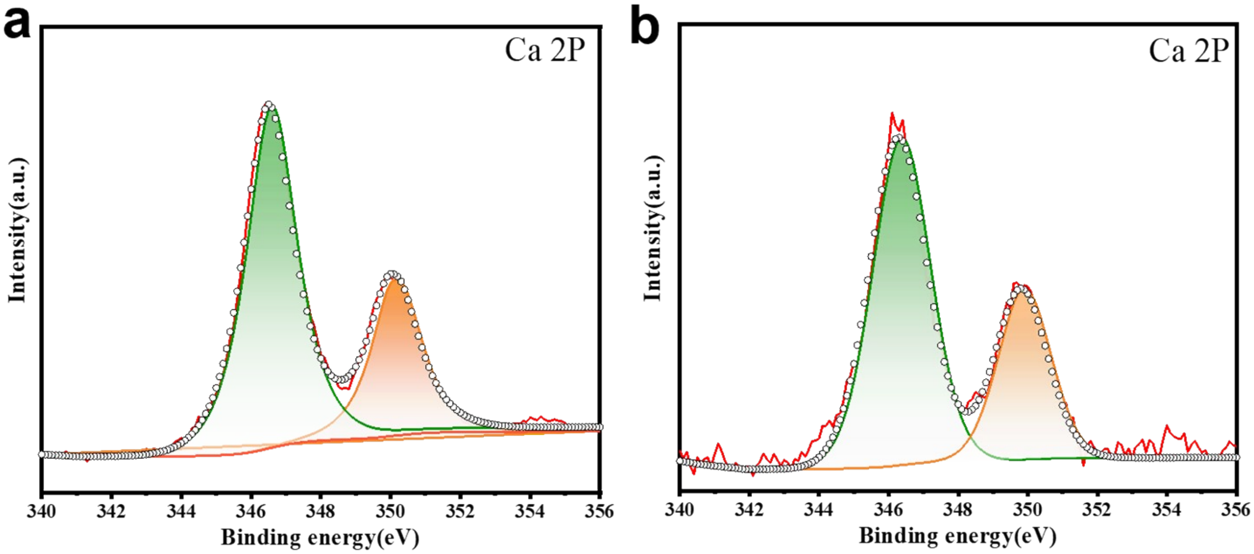

Fig. S29. XPS patterns and fitting results of Ca 2p of a) Tu-NCP@333 and b) HT-NCP@333.

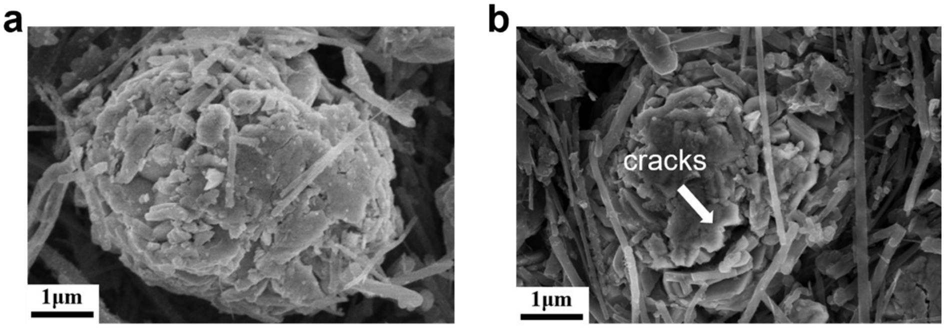

Fig. S30. SEM images for the a) HT−NCP@333 and b) Tu−NCP@333 cathodes after 500 cycles.

Table S1. Table of $[Ni_{1/3}Fe_{1/3}Mn_{1/3}](OH)_2$ particle size distribution of precursors (μm)

D10	D50	D90
3.58	6.21	7.50

Table S2. ICP-OES results of as-prepared HT-NCP@333 and Tu-NCP@333

Theoretical chemical formula	Composition from ICP					
	Na	Ni	Fe	Mn	Ca	P
Tu-NCP@333	0.98	0.322	0.34	0.34	2.7%	1.1%
HT-NCP@333	1.01	0.325	0.33	0.335	2.8%	1.2%

Table S3. Crystallographic and Rietveld refinement data of the as-prepared Tu-333 cathode by XRD data.

Space group: R-3m		Rp = 3.44%	Rwp = 2.73%	χ^2=1.22
a (Å)	2.98801		α (°)	90
b (Å)	2.98801		β (°)	90
c (Å)	15.95744		γ (°)	120
Atom	X	Y	Z	Occ
Na1	0	0	0	0.9935
Ni1	0	0	0.5	0.33
Mn1	0	0	0.5	0.32718
Fe1	0	0	0.5	0.33
O1	0	0	0.231	1

Table S4. Crystallographic and Rietveld refinement data of the as-prepared HT-333 cathode by XRD data.

Space group: R-3m		Rp = 2.13%	Rwp = 1.08%	χ^2=1.27
a (Å)	2.98146		α (°)	90
b (Å)	2.98146		β (°)	90
c (Å)	16.00984		γ (°)	120
Atom	X	Y	Z	Occ
Na1	0	0	0	0.995
Ni1	0	0	0.5	0.33
Mn1	0	0	0.5	0.33
Fe1	0	0	0.5	0.33
O1	0	0	0.231	1

Table S5. Refined crystallographic parameters for synchrotron XRD pattern of Tu-NCP@333

Space group: R-3m		Rp = 6.6%	Rwp = 4.8%	χ^2=1.67
a (Å)	2.985019		α (°)	90
b (Å)	2.985019		β (°)	90
c (Å)	15.63334		γ (°)	120
Atom	X	Y	Z	Occ
Na1	0	0	0	0.98327
Ni1	0	0	0.5	0.31671
Mn1	0	0	0.5	0.32034
Fe1	0	0	0.5	0.32907
O1	0	0	0.22253	1

Table S6. Refined crystallographic parameters for synchrotron XRD pattern of HT-NCP@333

Space group: R-3m		Rp = 4.6%	Rwp = 2.3%	χ^2=1.43
a (Å)	2.983189		α (°)	90
b (Å)	2.983189		β (°)	90
c (Å)	16.02625		γ (°)	120
Atom	X	Y	Z	Occ
Na1	0	0	0	0.98
Ni1	0	0	0.5	0.33
Mn1	0	0	0.5	0.33
Fe1	0	0	0.5	0.33
O1	0	0	0.21261	1

Table S7. DRT peaks and corresponding kinetic processes

Peak	Time constant	Kinetic process
D1	10^{-5}	The contact resistance between the material and the current collector
D2~D3	10^{-4}~10^{-2}	the solid electrolyte interface (SEI) impedance of both graphite and the counter electrode (lithium metal)
D4	10^{-2}~1	the transfer of lithium ions to the electrode surface
D5	1~10	the sodium ion intercalation process

Table S8. Pouch-type cell parameters

	Component	Mass
Cathode	HT-NCP@333	3.8 g
	Super P	0.21 g
	PVDF	0.21 g
	Al foil×4 pieces	0.2g×4=0.8 g
Anode	HC	1.54 g
	Super P	0.085 g
	Sodium Alginate	0.085 g
	Al foil×3 pieces	0.2g×3=0.6 g
Separator + Tabs	Celgard separator	0.25 g
Package	Al plastic film	2.5 g
Electrolyte	$NaPF_6$ in EC + DEC	2 mL=2.2 g
Total pouch battery mass 12.24 g	Energy 1.41 Wh	Energy density 115 Wh kg^{-1}